

Title: Force sensing to reconstruct potential energy landscapes for cluttered large obstacle traversal

Authors: Yaqing Wang, Ling Xu, Chen Li*

Affiliations: Department of Mechanical Engineering, Johns Hopkins University, Baltimore, MD

*Corresponding author, <https://li.me.jhu.edu>

Abstract:

Visual sensing of environmental geometry allows robots to use artificial potential fields to avoid sparse obstacles. Yet robots must further traverse cluttered large obstacles for applications like search and rescue through rubble and planetary exploration across Martian rocks. Recent studies discovered that to traverse cluttered large obstacles, multi-legged insects and insect-inspired robots make strenuous transitions across locomotor modes with major changes in body orientation. When viewed on a potential energy landscape resulting from locomotor-obstacle physical interaction, these are barrier-crossing transitions across landscape basins. This potential energy landscape approach may provide a modeling framework for cluttered large obstacle traversal. Here, we take the next step toward this vision by testing whether force sensing allows the reconstruction of the potential energy landscape. We developed a cockroach-inspired, minimalistic robot capable of sensing obstacle contact forces and torques around its body as it propelled forward against a pair of cluttered grass-like beam obstacles. We performed measurements over many traverses with systematically varied body orientations. Despite the forces and torques not being fully conservative, they well-matched the potential energy landscape gradients and the landscape reconstructed from them well-matched ground truth. In addition, inspired by cockroach observations, we found that robot head oscillation during traversal further improved the accuracies of force sensing and landscape reconstruction. We still need to study how to reconstruct landscape during a single traverse, as in applications, robots have little chance to use multiple traverses to sample the environment systematically and how to find landscape saddles for least-effort transitions to traverse.

One Sentence Summary:

Contact forces sensing allows reconstruction of potential energy landscapes for robot traversal of cluttered large obstacles.

INTRODUCTION

Sensing facilitates locomotor planning and control in mobile robots and animals (**Fig. 1A, B**). For example, sensors that enable machine vision (e.g., cameras, radars, LiDAR (*1*)) to provide a geometric map of the environment (*2–6*). Based on this map, the robot can construct a navigation function (*7, 8*) (or an artificial potential field (*9*)), with high potential regions representing obstacles and low potential minimum representing its goal, and plan and follow a gradient descent path to reach a goal while avoiding sparse obstacles (*10–13*). To help legged robots follow planned paths, studies in animal sensorimotor control and bio-inspired robots show that animals and robots use tactile and proprioceptive sensing as feedback signals to controllers that stabilize running and walking around limit cycles (*14–20*). These advances have greatly facilitated legged robot locomotion on flat ground and terrain with small obstacles (unevenness $\ll 1$ leg length) (*21*).

Further enabling legged robots to traverse even larger obstacles (comparable to body size) by physically interacting with them will extend their accessible terrains and facilitate important applications, such as search and rescue in rubble (*22, 23*), environmental monitoring through natural terrain (*24, 25*), and planetary exploration through large Martian rocks (*26–28*). Recent systematic research of the forest floor-dwelling discoid cockroach and its robotic models traversing diverse types of large obstacles presenting distinct locomotor challenges have begun to reveal physical principles. The animal or robot can self-destabilize far away from limit-cycle-like walking and running by physically interacting with the obstacles to transition across different locomotor modes—effectively finding easier pathways—to traverse cluttered large obstacles (*29–31*). The body-obstacle physical interaction results in a potential energy landscape. Locomotor modes emerge as the system was attracted to landscape basins separated by potential energy barriers (*21, 30–32*). Thus, the locomotor transitions are strenuous barrier-crossing transitions between landscape basins. Some modes can lead to traversal, while others lead to being trapped (*21, 30–33*). To facilitate transitions across modes to traverse, the animal or robot can generate kinetic energy fluctuation from oscillatory self-propulsion, which helps stochastically overcome the barrier to escape from one basin

and reach another(31). They can also actively adjust their bodies and appendages to facilitate locomotor transitions by steering on the landscape, modulating the transition barrier, or even adding/removing basins (32–35). Analogous to the artificial potential fields and navigation functions as a foundation for sparse obstacle avoidance using geometry-based environmental maps, we envision that this potential energy landscape approach will provide mechanics-based environmental maps for robots to compose locomotor transitions across modes to traverse heterogeneous cluttered large obstacles (for a review, see (30)).

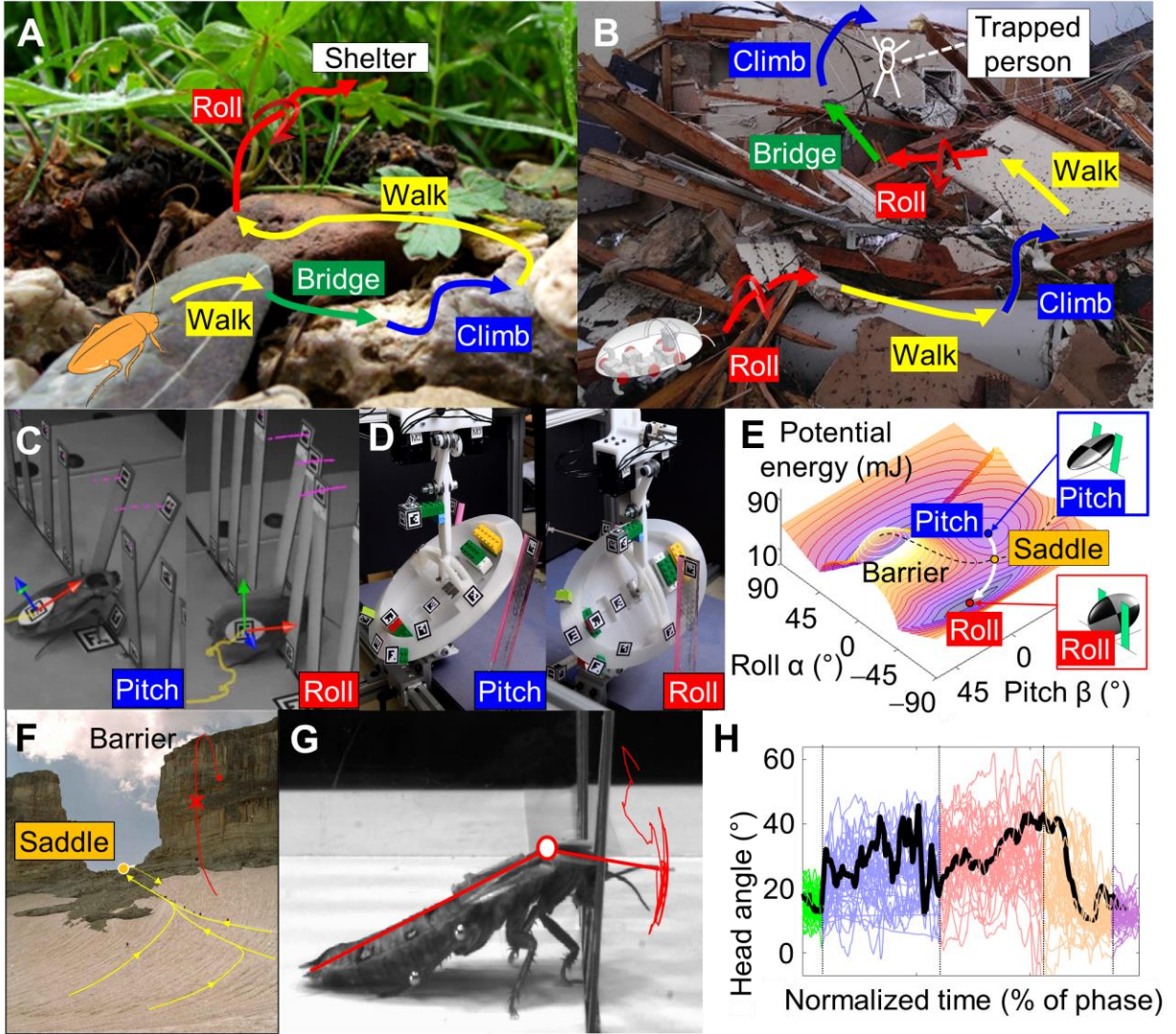


Fig. 1. Locomotor transitions of animals and robots in complex terrain and active sensing behavior.

(A and B) Illustrative locomotor transitions of (A) a cockroach traversing rugged natural terrain and (B) a robot traversing an earthquake rubble for search and rescue. (C) Cockroaches traversed cluttered grass-like

beams with small gaps ($<$ body width). They often transition from pitching up against the beams (left, blue) to rolling through the gap (right, red) (31). **(D)** A minimalist, feedforward robot can use kinetic energy fluctuation of body oscillation to cross the barrier to make a transition from pitch (left, blue) to roll mode (right, red), even without planning. **(E)** A snapshot of potential energy landscape over body pitch-roll space resulting from body-obstacle physical interaction (when the body is close to the obstacles), with a pitch basin and a roll basin separated by a potential energy barrier. The animal/robot's pitch or roll (A) mode emerges as the system is attracted to the pitch or roll basin (31). To traverse, the animal/robot must escape entrapment in the pitch basin/mode, cross the potential energy barrier, and reach the roll basin/mode (31). White arrow shows least-effort transition from pitch (blue) to roll (red) basin via the saddle point (orange) on the potential energy barrier (black dashed curve). **(F)** A metaphor of locomotor transition using a mountain climbing example. To climb over a mountain effectively, people go to the saddle point (yellow arrows) instead of climbing up large barriers (red arrow). Similarly, locomotor transition meets minimum efforts by transitioning via the saddle point. **(G)** A snapshot of a cockroach oscillating its head to traverse cluttered large obstacles. Red curve shows representative head oscillation from a trial. **(H)** Head flexion as a function of time when cockroach traversed cluttered large obstacles. Colors are for the five phases of approach (green), explore + pitch (blue), roll (red), land (orange), and depart (purple). Colored curves are individual trials from (35). Thick black curve is one example trial. This figure shows that the animal continuously oscillated its head while negotiating with the beams in the explore + pitch and roll phases. (A-D, F) are adapted from (31). (E) is from an online resource. (G, H) are adapted from (35).

Toward this vision, we take the next step by studying whether a robot can use obstacle contact force sensing to estimate potential energy landscapes. Because the potential energy landscape results from physical interaction (forces), vision-based sensing is insufficient for estimating it. Thus, robots need contact force sensing (36). In addition, because locomotor mode transitions in cluttered large obstacles involve large changes in body orientation, the potential energy landscape includes rotational dimensions (30, 31). Thus, robots also need to obtain torques from contact forces. The system's potential energy is the integral of conservative external forces and torques along relevant degrees of freedom, $PE(X) =$

$-\sum_i \int_{X_i(0)}^{X_i} q_i(X) dX_i$, where PE is potential energy (which includes gravitational potential and elastic potential energy), $X = (x, y, z, \text{roll}, \text{pitch}, \text{yaw})$ is the state vector, and q is the generalized force. Because gravitational force and its torques can be relatively easily obtained, if a robot can measure conservative forces and torques resulting from obstacle interaction (i.e., landscape gradients), it should be able to reconstruct the potential energy landscape.

Furthermore, because locomotor transitions to traverse cluttered large obstacles are strenuous, it helps a robot (or an animal) to find and cross saddles between landscape basins to make the least-effort transitions. If a robot (or animal) can sense landscape gradients, it may be able to start from one basin (one locomotor mode), perform gradient ascent while following the smallest gradient paths (i.e., gradient extremal path (37, 38)) to find and cross the saddles, to reach another basin (transition to another mode). This is in stark contrast to the gradient descent algorithms (39) that guide robots towards a minimum at the goal in the navigation functions or artificial potential field approaches for sparse obstacle avoidance.

Unlike long-range vision that can obtain a large geometric landscape and guide a robot or an animal to cross the saddle of a visible barrier (e.g., a mountain ridge, **Fig. 1F**) for least-effort traversal, reconstructing potential energy landscapes to identify saddles of potential energy barriers (which often do not correspond with geometric barriers (30–34)) requires sensing forces and torques over a range of the relevant degrees of freedom because such sensing requires contacting the obstacles. Curiously, the discoid cockroach often exhibits up/down head oscillations (not present during locomotion on flat ground (35), **Fig. 1G, Fig. 1H**, also see Section **S6**) and large body translational and rotational oscillations (more than on flat ground (35)) while pushing against large obstacles, before transitioning to easier modes to traverse (29, 31, 32, 35). We speculate that, besides providing kinetic energy fluctuation to stochastically cross potential energy barriers (31), such motions are also “exploratory” (40) and help the animal sense landscape gradients over a small range of states around the current state and allow it to identify and follow locally smallest gradient directions to eventually find and cross saddles.

To begin to explore these intriguing questions, we created a cockroach-inspired, minimalistic robot capable of sensing forces and torques from obstacle contact around its body as a simplified robophysical model (41–49) for systematic laboratory experiments. As a first step, in this study, we tested how well sensing obstacle contact forces and torques (which are not fully conservative) allows the robot to estimate landscape gradients and reconstruct the potential energy landscape in the simplest case of using many traverses with prescribed trajectories to sense forces and torques over a broad range of relevant states systematically (which is feasible in the lab but less so in real applications). We also used the robot to systematically study whether adding head oscillation enhances sensing landscape gradients and reconstructing the landscape. Ultimately, we hope to build on this initial sensing and landscape reconstruction work to enable self-propelled, free-moving robots, during a single, “zero-shot” (50) traverse with substantial sensing noise, to use a range of exploratory motions to sample forces and torques around its current state, estimate and follow the lowest gradient direction and follow it to gradually find saddles, and control its self-propulsion to cross saddles to make least-effort transitions to traverse cluttered large obstacles.

Our study builds on our previous model system of grass-like beam traversal (29–31, 35) (**Fig. 1C, D, Fig. 3A**). To traverse relatively stiff cluttered beam obstacles with gaps narrower than their body width, the discoid cockroach and legged robots inspired from it often transition from a strenuous pitch mode (pushing forward across beams with large body pitching), which requires a large force and energy cost (**Fig. 1C, D, blue**) to a much easier roll mode (rolling into beam gaps and maneuvering through forward), which requires a much smaller force and energy cost (**Fig. 1C, D, red**). This pitch-to-roll transition is from a pitch basin to a roll basin on the potential energy landscape over body pitch and roll (**Fig. 2B, blue and red**). These basins emerge and morph as the body moves forward, changing the pitch-to-roll transition potential energy barrier (**Fig. 2B, ii, iii, gray dashed curve**).

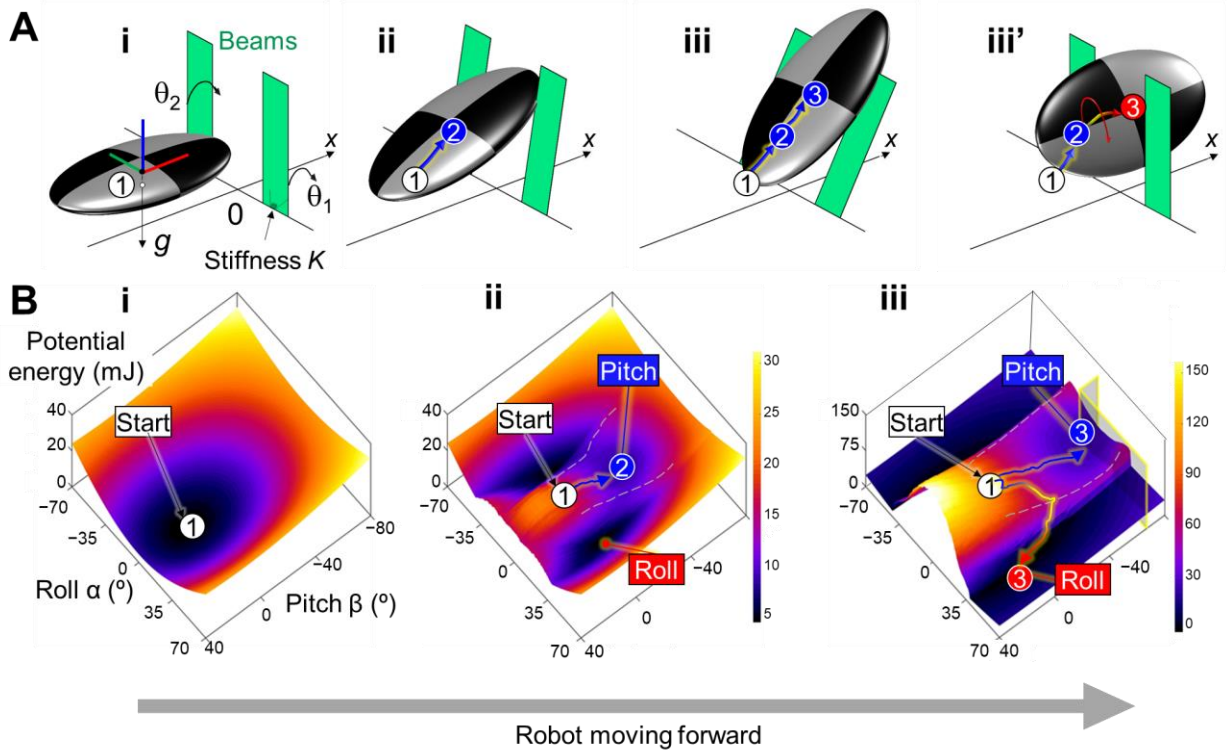


Fig. 2. Robot locomotor transitions on a potential energy landscape. (A) Snapshots of a robot before and during interaction with two beams in pitch (I, ii, and iii) and roll (iii') modes. (B) Snapshots of landscape over pitch-roll (α - β) space before (i) and during (ii and iii) interaction. Representative system state trajectories are shown for staying in pitch basin (blue) and transitioning to roll basin (red). The dashed gray curves on landscape show boundaries between pitch and roll basins. Adapted from (31).

RESULTS

New robot capable of obstacle force and torque sensing

To systematically study landscape gradient sensing and landscape reconstruction, we iteratively developed and refined (**Fig. S1**) a minimalistic cockroach-inspired robot with the ability to sense contact forces around its body (**Fig. 3B**) while moving forward at a constant speed with prescribed body pitch and roll, which can be varied across trials. Our robot system design follows the previous sensor-less robot for studying the passive dynamics of the system (31). The system (**Fig. 3A**) consisted of a simple shield-shaped

body similar to the discoid cockroach's body shape traversing a pair of deflectable beams (**Fig. 3A**), each with a pin joint at the base with a relatively stiff torsion spring, which mimics the cockroach traversing grass-like obstacles. The actual shield-shaped body was cropped from a full shield shape (**Fig. 3C**, translucent green) to enable head oscillation (as a full shield shape would result in body-head overlap). The front of the shell was also cropped, only reserving the part where the beam contact happened. The body was driven forward by an external translational motor to emulate the forward propulsion generated by legs, but without adding legs. The previous robot's body was suspended via a low-friction gyroscope mechanism to allow pitch and roll. The body was bottom-heavy so that it could passively settle into a horizontal posture (zero pitch, zero roll) under gravity when not interacting with obstacles. This emulated a cockroach or multi-legged robot running on level, flat ground having a near horizontal body posture because this posture is the most stable (i.e., system potential energy landscape has a global minimum at zero pitch and zero roll). For systematically measuring obstacle contact forces and torques over a broad range of body pitch and roll, we added two motors to rigidly attach to the body to prescribe body pitch and roll (i.e., disabled the previous gyroscope mechanism that allows free pitching and rolling).

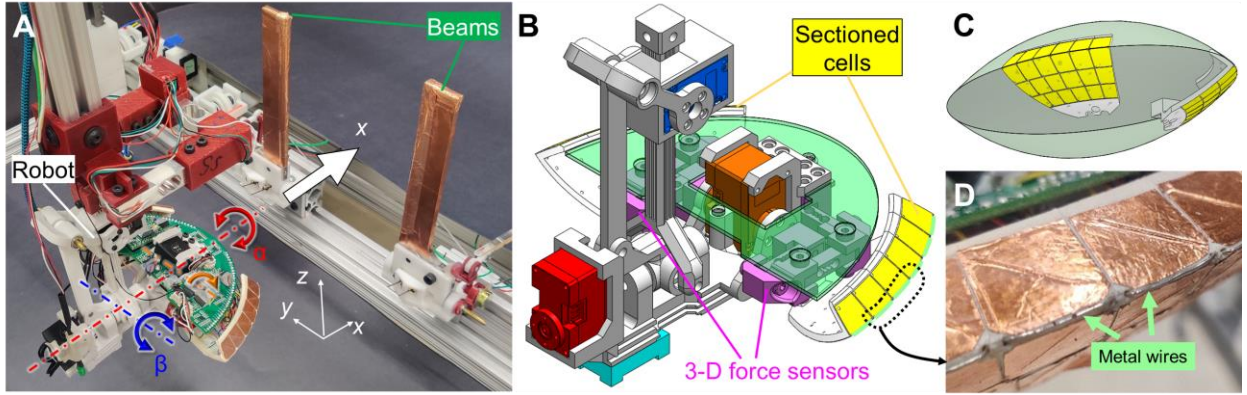


Fig. 3. Design of experimental system and robotic physical model. (A) Photo of the experimental system consisting of a robot, a vertical gantry crane structure, and beams. x , y , and z axes show lab frame. The robot is propelled forward along $+x$ direction at a constant speed (white arrow); at the same time, its roll (red arrows), pitch (blue arrows), and head rotation (orange arrow) are fully actuated by servo motors. (B)

CAD model of robot. (C) Shell shape design. The shell was cropped from a shield-shaped counterpart (translucent green). (D) Metal wires on the edge as touch sensory cells.

Obstacle contact force sensing was achieved by a custom 3-axis force sensor, and torque sensing was achieved by further adding touch sensory cells over the body to sense contact position with both beams. To measure the contact force with either beam separately, the robot’s outer shell was separated into a left and a right part. We connected each piece of shell with the head frame via a custom small, low-cost 3-axis force sensor (**Fig. 3B**, magenta). The small size of the custom sensor (58 mm \times 44 mm \times 22 mm) suited the compact design of our robot, as opposed to other commercial ones. Each force sensor consisted of three load cells serially connected and orthogonal to each other. To detect the contact position with each beam, we attached sectioned cells made of copper tape (51) (**Fig. 3B, C**, yellow) on the shell surface. To detect the edge contact (i.e., a beam contact at the sharp edge), the edge was separated into six sections; each was covered by a piece of metal wire as a cell (0.5 mm in diameter, **Fig. 3B, C**, mint, **Fig. 3D**).

Sensor range and spatial resolution

Each load cell in the force sensor provided a separate force measurement along the robot’s x -, y -, or z -axis, with a range of ± 20 N and a precision of ± 0.004 N, which suited our experiment in which the contact forces were < 10 N. See Section S4 for force sensor calibration.

The pattern of the touch sensory cell distribution was carefully designed so that the measurement error of contact position (defined as the distance between the exact contact point and the estimation) and normal direction (defined as the angle between the normal direction at the contact and the estimation) were within a small threshold (i.e., position error < 25 mm, normal direction error $< 5^\circ$, not including the edge contact case). See S1 for how we selected force sensors, added contact point sensing, and gradually improved touch sensor resolution in the iterative robot development process.

Trends of contact forces and torques matched with the landscape gradients

To estimate the potential energy landscape over the space of fore-aft translation (x) and roll (α) and pitch (β) rotation, we controlled the robot sweep this space. The robot’s body pitch and roll were set to the desired values before each trial, and then it traversed the beam obstacles while sensing the 3-D raw contact

force (**Fig. 4A**, red) and contact position (**Fig. 4A**, orange) at 50 Hz. We calculated the torque that each beam's contact force exerted on the robot's geometric center as its raw contact torque (see Section **Force analyses** in **Materials and Methods**). We observed several trends of the measured forces and torques (**Fig. 4B, C**) in the x - α - β space, namely, the fore-aft force F_x , roll torque T_α , and pitch torque T_β . (1) The fore-aft force was always negative (averaged $F_x = -2.0 \pm 0.4$ N) when the robot contacted the beams. (2) For a small roll angle ($\alpha = 0^\circ - 30^\circ$), the roll torque was near-zero (averaged $T_\alpha = 7 \pm 17$ N·mm). (3) For a large roll angle ($\alpha = 35^\circ - 40^\circ$), the roll torque was positive (maximum $T_\alpha = 98 \pm 66$ N·mm) at first, but then suddenly reduced to negative (minimum $T_\alpha = -41 \pm 45$ N·mm). (4) For a small pitch angle ($|\beta| = 10^\circ - 20^\circ$), the pitch torque was positive (maximum $T_\beta = 27 \pm 22$ N·mm) at first, but then reduced to negative (minimum $T_\beta = -98 \pm 46$ N·mm). (5) For a large pitch angle ($|\beta| = 25^\circ - 40^\circ$), the pitch torque was always negative (averaged $T_\beta = -45 \pm 20$ N·mm).

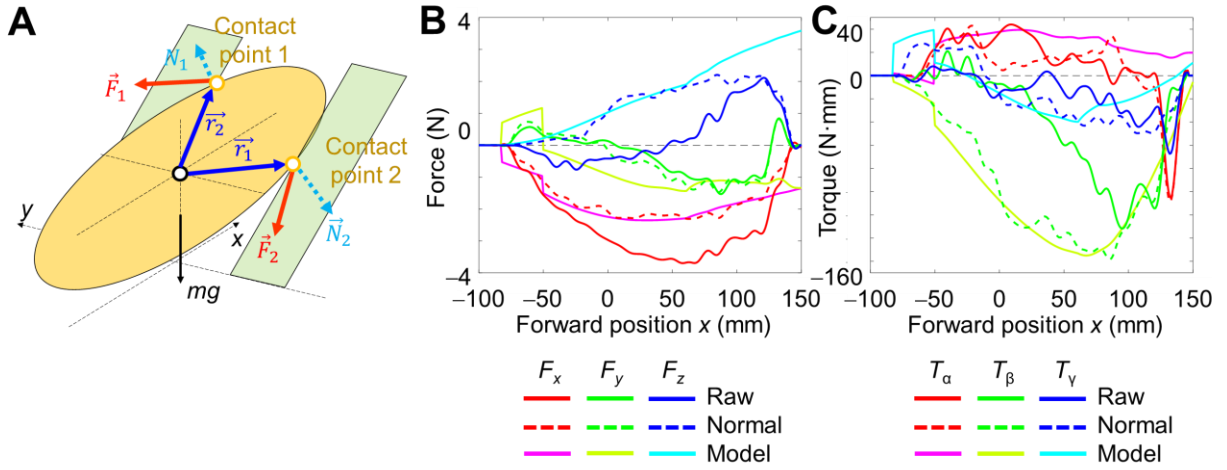


Fig. 4. Estimating the potential energy landscape gradients using measured contact forces and torques. (A) Schematic of force analyses. The robot directly obtained the measured raw contact forces F_i (red arrows) from custom 3-D force sensors and contact positions (orange points) from touch sensors. Normal forces N_i (cyan arrows) were defined as the component of contact forces along surface normal directions. Force arms r_i (blue arrows) were the distance from the geometric center to the contact point. Raw or normal torques were the cross of force arms and raw ($T_i = r_i \times F_i$) or normal forces ($T_{i,N} = r_i \times N_i$),

separately. **(B)** Raw, normal, and model contact **(i)** forces and **(ii)** torques as functions of forward position x from a representative trial.

Here, we further describe the evolution of the potential energy landscape as the robot traversed the beam obstacles (**Fig. 2**) to help understand how these observed trends matched with the those expected from the landscape. We defined the potential energy landscape similarly as in (31) (see Section *Potential energy landscape modeling* in *Materials and Methods* and section **S1**). Before encountering the beams, the system’s potential energy was simply the body’s gravitational potential energy. Because the robot was bottom-heavy, the potential energy landscape formed a basin in the roll-pitch (α - β) section, whose global minimum was at zero pitch and zero roll (i.e., the horizontal posture, $\alpha = \beta = 0^\circ$). As the robot encountered and interacted with the beams, the average potential energy landscape in α - β section lifted, because more beam elastic energy was stored, and the system potential energy increased. The global basin evolved into a “pitch” basin, whose local minimum was at a negative pitch ($|\beta| = 0^\circ - 70^\circ$) and zero roll. At the same time, two “roll” basins emerged, whose local minima were at near-zero pitch and a positive or negative roll (around $\alpha = \pm 50^\circ$). The separation of the pitch and roll basins were around $\alpha = \pm 35^\circ$ (**Fig. 1E**).

Comparing the trends of measured forces and torques with landscape evolution, we found that the direction of contact forces and torques along x , α , and β directions were always inverse to the corresponding landscape gradients. Specifically, (1) the system potential energy increased with x (**Fig. 2B**, **video S1**), suggesting a positive gradient along the x direction. (2) the landscape gradients were near-zero when the robot’s state felled in the pitch basin and was near the local minimum (**Fig. 2B**, blue) at a small roll angle (3) the landscape gradients along α direction was initially negative when the robot’s state was in the roll basin to the $+\alpha$ side of the barrier (**Fig. 2B**, red) at a large roll angle. (4, 5) The landscape gradients along β direction were initially negative when the robot’s state was to the $-\beta$ side of the local pitch or roll minimum. As the robot moved forward, if $|\beta|$ was small, the landscape gradients along the β direction changed to positive as the landscape minimum shifted along $-\beta$ direction and passed the robot’s state.

The match between the trends of forces and torques and the landscape evolution suggested that the contact forces and torques were strongly related to the corresponding landscape gradients. We did not find a match between the landscape evolution with the sudden reduction in roll torque in (3) because, after the robot detached from the left beam, the system is beyond the assumption of this simple landscape modeling (31).

Contact forces and torques matched landscape gradients

We further quantitatively compared the contact forces and torques with the landscape gradients from modeling and found that they partially matched each other (**Fig. 4B**, raw vs. model, **Fig. 7A-C**, raw, **Table 1**). The contact forces and torques matched the landscape gradients, with a small relative error of $e_x = 15\% \pm 3\%$ in the x direction, $e_\alpha = 19\% \pm 28\%$ in the roll direction, and $e_\beta = 25\% \pm 9\%$ in the pitch direction (see Section *Comparison criteria and Statistics* in *Materials and Methods* for the definition of relative error).

These results showed that, despite not being fully conservative, the contact forces sensed enabled potential energy landscape gradient estimation. We speculated that the mismatch between the sensed forces and torques and the landscape gradients was from friction, collisions, inertia effect, etc. See Section **S2** for theoretical proof that the contact force and torque should be the landscape gradients without these factors.

Reconstruction of potential energy landscape

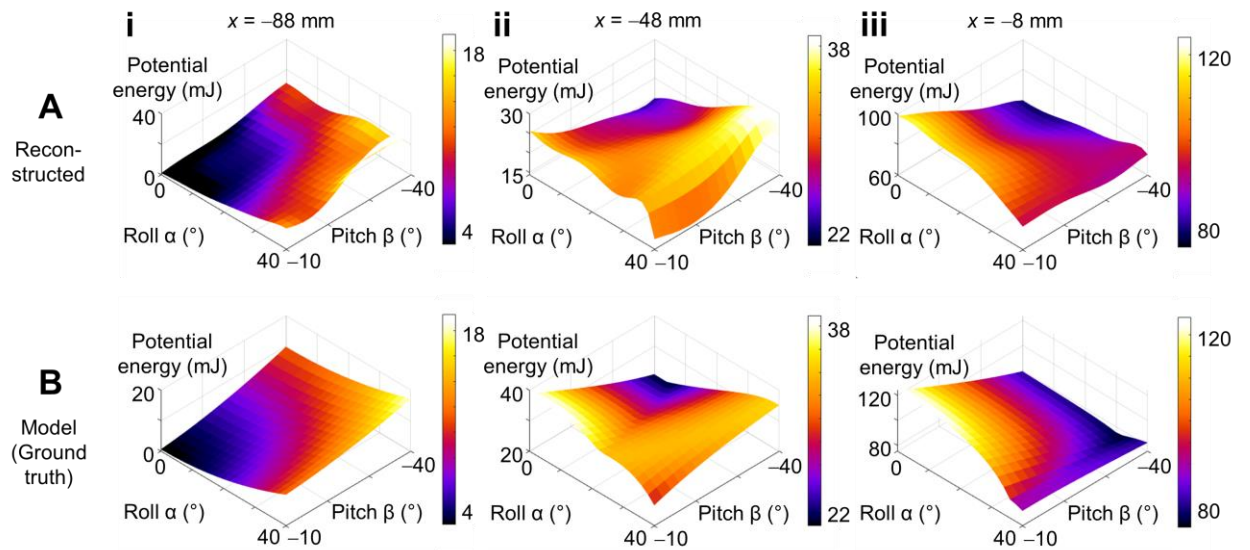


Fig. 5. Comparison of reconstructed and modeled potential energy landscape. (A) Potential energy landscape evolved as the robot moved forward. (a) Reconstructed landscape from measured data. (b) Ground truth from modeling. In (a and b), the landscape is from the trials without head oscillation ($f = 0$ Hz) as a demonstration. (i) $x = -88$ mm, (ii) $x = -48$ mm, (iii) $x = -8$ mm. The landscape figures in the same column share the same colormap range.

To test whether the contact force and torque sensing can infer the potential energy landscape, we used the sensed forces and torques to reconstruct the landscape (see Section *Potential energy landscape reconstruction* in *Materials and Methods*). We found that the reconstructed landscape and its gradients matched the ground truth from modeling (**Fig. 5, Fig. 7D, E, raw, Table 1**) with a low relative error of $e_{PE} = 14.03\% \pm 0.03\%$ in energy and $e_{Grad} = 21.6\% \pm 0.7\%$ in gradients (see Section *Comparison criteria and Statistics* in *Materials and Methods* for the definition of relative error).

By comparison, we also reconstructed the potential energy landscape using vision-based geometry sensing by assuming that beams are rigid (see section S3), which had a much poorer reconstruction accuracy (relative error in energy $e_{PE} = 180\%$). These results showed that the contact forces sensing enabled potential energy landscape reconstruction.

Using normal force sometimes enhances gradient estimation and landscape reconstruction accuracy

Because friction could be one of the factors that caused a mismatch between sensed forces and torques and the landscape gradients, we used normal forces (i.e., the component of raw contact forces on the surface normal direction) and their torques to estimate landscape gradients to eliminate the effect from friction (component on the surface tangential direction) (see Section *Force analyses* in *Materials and Methods*). We found that the normal forces and torques well matched the landscape gradients (**Fig. 4B, normal vs. model**). Using the normal forces and torques improved matching in the x direction with $e_x = 5\% \pm 3\%$ ($p < 0.001$, Student's t-test) (**Fig. 7A, Table 1**), but worsened matching in the β direction with $e_\beta = 31\% \pm 9\%$ ($p < 0.01$, Student's t-test) (**Fig. 7C, Table 1**). We also found that using normal forces and torques improved the accuracy of landscape reconstruction than the raw measurement with a smaller

relative error of $e_{PE} = 7.24\% \pm 0.02\%$ and $e_{Grad} = 17.7\% \pm 0.4\%$ ($p < 0.001$, Student's t-test) (**Fig. 7D, E**, normal vs. raw, **Table 1**).

These results showed that using normal forces and torques sometimes improved landscape gradient estimation and landscape reconstruction. Further discussion on why using normal forces and torques does not improve landscape gradient estimation in α direction and β direction for the shield-shaped robot are in the Section *Remaining issues in this study* in *Discussion*.

Effect of head oscillation on sensing and landscape reconstruction

Finally, to explore the potential function of the cockroach's active head oscillation, we controlled the robot to actively oscillate its head at various frequencies while traversing the beams and compared the raw contact forces and torques with the landscape gradients. To emulate the animal behavior, besides no head oscillation (data already described above, 0 Hz in **Fig. 7**), we controlled the head oscillation frequency to 0.5, 1, and 2 Hz (see Section **S6** for frequency selection). We found that as the head oscillation frequency increased, the measured raw forces and torques sometimes converged to the model (**Fig. 6**), especially at a small roll angle. In the range of head oscillation frequency that we tested ($f = 0 - 2$ Hz), the contact forces and torques along x and β directions better matched the model as the frequency increased ($p < 0.001$, Kruskal-Wallis test) (**Fig. 7 A-C**, raw, shield-shaped). We also reconstructed the potential energy landscape and found that, in the range of head oscillation frequency that we tested ($f = 0 - 2$ Hz), the reconstructed landscape better matched the ground truth in energy and gradients as frequency increased ($p < 0.001$, Kruskal-Wallis test) (**Fig. 7 D, E**, raw, shield-shaped).

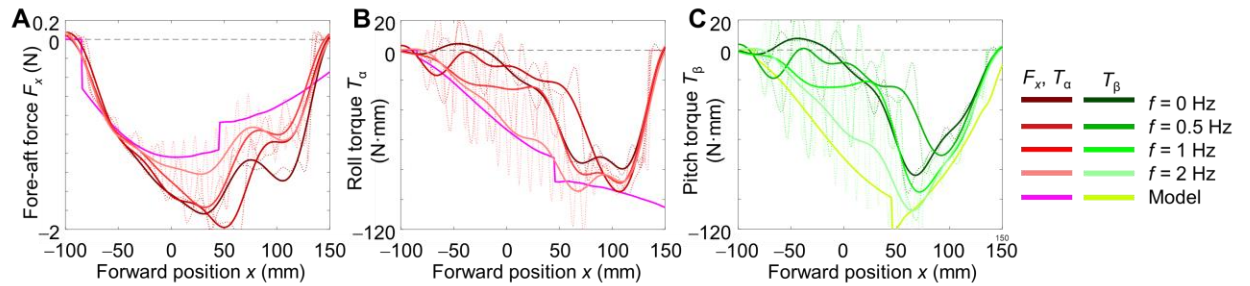


Fig. 6. Contact forces and torques from various head oscillation frequencies. (A) Fore-aft force F_x , **(B)** roll torque T_α , and **(C)** pitch torque T_β as functions of forward position x from a representative trial. As the

total roll torque was near zero, we show the forces and torques from contact with the right beam only to better show the comparison. Thin, dashed curves are original filtered data (see Section *Data filtering and averaging*). Thick, solid curves are further processed by zero-phase digital filtering using a six-order Butterworth filter with a cut-off frequency of 1 Hz for better comparison.

These results showed that active head oscillation sometimes improves landscape gradient estimation and could facilitate landscape reconstruction compared to without oscillation.

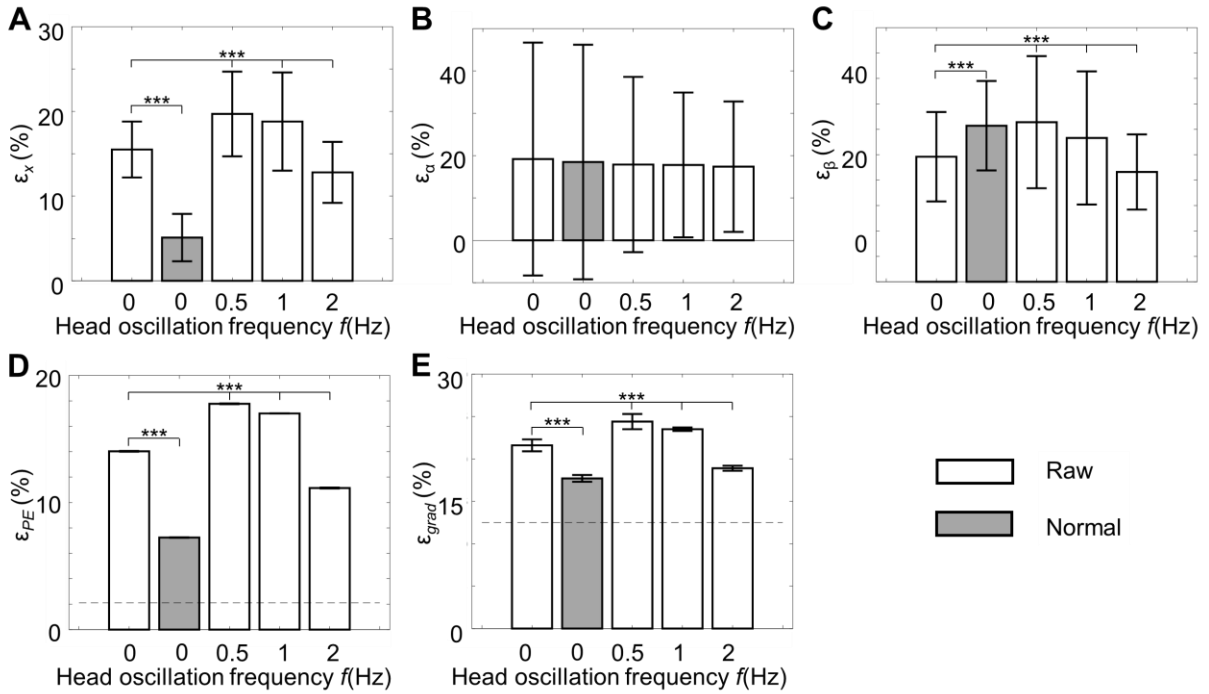


Fig. 7. Relative error of potential energy landscape gradient estimation and landscape reconstruction. (A, B, and C) are relative error ϵ_x , ϵ_a , and ϵ_β of using measured (A) fore-aft force F_x , (B) roll torque T_a , and (C) pitch torque T_β as the landscape gradients, separately. (D and E) are relative error ϵ_{PE} and ϵ_{grad} of potential energy and gradients in landscape reconstruction. See Section *Comparison criteria and statistics* in *Materials and Methods* for the definition of relative error. Bars and error bars are means ± 1 standard deviation of the average relative error of all average trials. *** $P < 0.001$, ** $P < 0.01$, Student's t-test for comparing raw and normal forces or torques, Kruskal-Wallis test for comparison among various head oscillation frequencies. Brackets and asterisks show important comparisons described in *Results*.

DISCUSSION

Major findings

In summary, we built a robot capable of sensing obstacles, contact forces, and torques. Using a model system of grass-like beam obstacle traversal, we found that such sensing enabled the potential energy landscape gradient estimation and landscape reconstruction, despite the sensed forces and torques not being fully conservative. We also found that using the normal component of the sensed contact forces improved the accuracy of gradient estimation and landscape reconstruction.

Why normal forces and their resulting torques well capture landscape gradients

In the robot experiment, the robot held its rotation and moved forward at a constant speed. We speculate that in that case, the system was dominated by conservative forces, whereas speed-dependent forces (damping) and inertial forces were small. The robot’s contact force with the beam mainly consisted of normal force and friction. Under kinetic Coulomb friction assumption, the direction of normal force should be parallel to the landscape gradients, while the friction should be perpendicular. To generate enough contact force to move or resist the beam bouncing back, the normal force should be roughly equal to the landscape gradients considering the work-energy principle.

Why head oscillation enhances sensing and reconstruction accuracy

We speculated that the fast head oscillation made the contact friction cancel out. When the robot’s head was static (relative to the body), under a kinetic Coulomb friction assumption, the contact friction f was along the direction of relative velocity \vec{v}_0 between the body and the beam, and its amplitude depended on the normal contact force N and friction coefficient μ : $f = \mu |N| \frac{\vec{v}_0}{|\vec{v}_0|}$. When the robot head oscillated up and down, it added an oscillatory velocity $\pm \vec{v}_{add}$ to the original relative velocity between the body and beams, and the contact friction was along the direction of this new relative velocity as $\vec{v}_1^\pm = \vec{v}_0 \pm \vec{v}_{add}$ for upward and downward head motion separately. As the head oscillation frequency increased, \vec{v}_{add} gradually dominated the relative velocity, which made the latter roughly the same amplitude and inverse direction in

the back- and forth- motion, $\overrightarrow{v_1^\pm} \approx \pm \overrightarrow{v_{add}}$, and so did the friction, which canceled out each other when averaged temporally. Thus, the sensed contact forces and torques were closer to the normal forces and torques that captured the landscape gradients better.

Besides improving force sensing and landscape reconstruction accuracy in the robotic experiment, this behavior may provide other benefits for the animal. See section *Head oscillation may allow active sensing of obstacle forces and torques* in *Discussion* for one likely function.

Head oscillation may allow active sensing of obstacle forces and torques

Previous biological studies in contact-based active sensing behavior (40, 52, 53) show that animals' force sensing inherently involves sensor motion, i.e., animals often move their sensors to enhance sensation. For example, when encountering an obstacle, an insect uses its antennae to repeatedly touch the obstacle (like a cockroach (54, 55)) or does an antenna search and sample behavior aided by body and head rotating (like a stick insect (56, 57)), which locates the obstacle and induces turning to avoid collision (54, 57, 58); a rat actively whisks (i.e., moving the whiskers back and forth) against objects when exploring the environment (59–62). From comparative robotic studies (63–65), this probably enables the animal to extract object contours (66, 67). We speculate that similarly, the discoid cockroach's head oscillation in beam obstacle traversal (31, 35) suggested a novel form of active sensing, which will be useful for freely moving robots traversing cluttered large obstacles.

To test this speculation, future studies should measure the animal's muscle activity and neural signals to first verify whether the behavior is active or passively resulting from obstacle interaction. If it is an active behavior, studies can collect more biological observations and use robophysical models to examine the function of this behavior.

How a free-running robot may use force sensing to facilitate transitions

We speculate that our strategy to sense contact forces and torques to estimate landscape gradients and reconstruct the landscape will work in free-running robots. Because traversing cluttered large obstacles is highly strenuous, the robot needs to continually push against and intermittently collide with them (30),

making it difficult to build up high momentum, i.e., it operates in a low-speed, small-acceleration regime, where the speed-dependent damping forces and inertial forces are likely small. Also, the robot often makes body contact with and pushes against the large obstacles (30), likely resulting in large normal forces, whereas the associated frictional forces are usually smaller. Based on these, it is plausible that the normal force dominates the noisy contact forces even for a freely running robot, and our approach still works.

Towards this, we still need to solve major additional questions. Firstly, how to filter the noisy contact force with the obstacle to infer the landscape gradients. When a self-propelled, free-moving legged robot (68) negotiates with obstacles, the force sensory data can be substantially noisy because of friction and damping, oscillation from cyclic leg propulsion, and impulse from frequent collision with the beams. Studies can look for better mechanical design or signal processing methods to try to obtain the landscape gradients and reconstruct the landscape from the noisy sensory data.

Secondly, how to use sensing to reconstruct the landscape near the robot’s trajectory to enable a single, “zero-shot” traversal. Future studies can adopt bio-inspired approaches. For example, cockroaches (29, 31, 35, 69) and ground beetles (70) often like to wedge in between obstacles like shrubs or rock cracks to go in to seek shelter. It is plausible that these animals use proprioceptive and tactile sensing (71, 72) to detect or infer the obstacle resistance or resistive forces as they do so (35). If this were the case, using such exploratory motions may allow these animals to sample contact forces and torques around its neighboring states and decide a direction with the least resistance to maneuver through/into the gaps/cracks. In other words, such animals’ preference to go towards weaker spots (if they have such preference) coupled with exploratory motions for force and torque sensing may lead them to follow small potential energy gradients to ascend towards saddles and make least-effort transitions (37, 38). We speculate that the robot can use a similar bio-inspired approach to actively sample around neighboring states to reconstruct a local landscape, estimate and follow the lowest gradient direction to gradually find saddles, and make least-effort transitions to traverse obstacles. Future studies can also adapt other numerical algorithms for finding saddles and maximum-likelihood transition paths between local stability basins in physical chemistry (38, 73–77).

Force sensing is useful for fully dynamic modeling of large obstacle traversal

Building on the potential energy landscape modeling, future studies should model the robot (and animal) locomotion during cluttered large obstacle traversal as a potential energy landscape-dominated, stochastically perturbed dynamics with diffusion (i.e., Langevin dynamics (78–80)), where friction, damping, kinetic energy fluctuation, and inertia effects will also be considered (30). The Langevin equations will greatly improve the prediction of the system dynamics, especially in the neighborhood of the saddle point, because around saddle points, the potential gradients are near zero, and the friction, damping, and oscillation will dominate the robot dynamics. Reliably producing Langevin dynamics models will improve our understanding of biological motion and create new possibilities for robot control in challenging environments.

Remaining issues in this study

Finally, a few issues in this study remain to be resolved or refined (also see Section S7). Firstly, the normal pitch torque matched the model worse than the raw one (**Fig. 7C**). We speculated that this was due to the wrong normal direction identification at an edge contact. Possible solutions could be better designing the robot and motion to avoid edge contact or scanning the geometry of the obstacle to decide the contact’s normal direction. Secondly, neither using normal torques nor involving head oscillation improved roll torque estimation (**Fig. 7B**). We speculated that this was because the pitch basin was flat along the roll direction, where the roll torque was near zero, and the friction-resulted torque dominated the measured pitch torque. We speculate that this can be better explained using Langevin dynamics (see Section *Force sensing is useful for fully dynamic modeling of large obstacle traversal* in *Discussion*). Finally, the landscape reconstruction did not show a steep gradient near the barrier like the ground truth (Fig 4, iii, around roll $\alpha = 35^\circ$). We speculate that this was because the state space of the steep gradient was small, and insufficient samples were taken in the neighborhood. A possible solution is to obtain more samples in the region with a steep gradient.

MATERIALS AND METHODS

Potential energy landscape modeling

The system's potential energy PE was the sum of the gravitational potential energy of the robot PE_G and the elastic potential energy from the beams PE_B :

$$PE_G = mg(\Delta z - h),$$

$$PE_B = \frac{1}{2} k_1 \theta_1^2 + \tau_1 \theta_1 + \frac{1}{2} k_2 \theta_2^2 + \tau_2 \theta_2,$$

$$PE = PE_G + PE_B = mg(\Delta z - h) + \frac{1}{2} k_1 \theta_1^2 + \tau_1 \theta_1 + \frac{1}{2} k_2 \theta_2^2 + \tau_2 \theta_2,$$

where m was the mass of the robot, g was the gravitational acceleration, Δz was the vertical distance between the geometric center and center of mass, $\theta_{1,2}$, $k_{1,2}$, and $\tau_{1,2}$ are the deflection angles, the torsional stiffness, and the preload of the left and right beams, separately. See Section **S1** for definition of variables and parameters.

Robot experiment protocol

Before each trial, the robot was positioned at a distance of 200 mm ($x = -200$ mm) from the beams, at a height of $z = 138$ mm, roughly in the midline ($y = -6$ mm) and pointing forward ($\gamma = 0^\circ$). The robot feed-forwardly rotated to the requested pitch and roll angle. The beams were set vertically and moved to have a gap of 130 mm wide symmetric to the midline. The robot's head was aligned with the body (head angle = 0°). All the force sensors were zeroed. Then, the robot's head started oscillating between 0° and 20° at a frequency of f (for $f > 0$) until the end of fore-aft translation, and the LabVIEW program started data recording. After a random period (to randomize the head oscillation phase), the robot was actuated to move forward at a constant speed of $20 \text{ mm} \cdot \text{s}^{-1}$ by a distance of 500 mm, which guaranteed the robot passed the beam obstacle area fully, and the beams were bounced back to vertical. Finally, we stopped the head oscillation and data recording and moved the robot back to its initial position for the next trial. Two cameras (Logitech C920 HD PRO, Logitech, Switzerland) synchronized by Open Broadcaster Software (OBS)

recorded the experiment from the side and the isometric views at a frame rate of 30 Hz and a resolution of 960×720 pixels.

We varied the head oscillation frequency f at 0, 0.5, 1, and 2 Hz. For each combination of shell type and head oscillation frequency f , we varied the desired roll angle α from 0° to 40° with an increment of 5° and the desired pitch angle β from -10° to -40° with a decrement of 5° (note that negative pitch angle meant pitching upward). At each combination of shell type, head oscillation frequency f , desired roll angle α , and pitch angle β , we performed five trials, which resulted in a total of $n = 1260$ trials.

Note that due to the robot frames and links were not excessively stiff, the robot's roll and pitch angle slightly changed (maximum roll change < 10°, maximum pitch change < 5°) in each trial. We measured the roll and pitch angles from IMU to account for this effect.

Force analyses

The raw contact forces (**Fig. 4A**, red) and contact positions (**Fig. 4A**, orange points) are directly measured from the sensors. To decide the normal direction at contact between the robot and beams, we considered two typical contact types. At a surface contact (i.e., the beam contacted the shell on its smooth 2-D surface, applied the later part of each trial), the normal direction was estimated as that of the touch detection sensor cell, which was obtained based on the full acknowledgment of the shell shape; at an edge-contact (i.e., the beam contacted the shell at its sharp 1-D front edge, applied to the former part of each trial for the shield-shaped shell), the normal direction was determined by both the robot's edge direction and the beam surface orientation. In this case, we assumed the normal direction vertical to the robot body z'' -axis and obtained a rough estimate. The normal force (**Fig. 4A**, cyan) was the component of the raw force along the normal direction. The force arm (**Fig. 4A**, blue) was the distance from the robot's geometric center to the contact position. The raw or normal torque was the cross of the force arm and the raw or normal force, separately. The raw or normal torques along the roll, pitch, and yaw direction were the projections of the torque T along the roll (X''), pitch (Y'), and yaw (Z) axes, separately. The total raw and normal forces and torques were the sum of those from the two beams. Note that in the force analyses section, we made no

assumption about the beam obstacle nor requested any obstacle properties or motion information, which indicates that these analyses are adaptable to various obstacles.

Data filtering and averaging

All the data (robot positions, orientations, head oscillation angles, forces, torques, etc.) were processed by zero-phase digital filtering (i.e., “filtfilt” function in MATLAB) using a six-order Butterworth filter with a cut-off frequency of 1.5 Hz ($f = 0$ Hz or 0.5 Hz), 3 Hz ($f = 1$ Hz), or 6 Hz ($f = 2$ Hz). To obtain the average data, we varied the x from -100 mm to 200 mm with an increment of 1 mm, and we linearly interpolated the measured data over x and then averaged them over the five repeated trials.

Potential energy landscape reconstruction

We used either the raw or normal contact forces and torques to estimate the vector field of landscape gradients in the x - α - β space, combining all averaged trials. Due to the slight change in the robot’s roll and pitch in each trial (see Section *Robot experiment protocol* in *Materials and Methods*), the vector field base was heterogeneous (i.e., not strictly gridded). We applied a meshless Helmholtz-Hodge decomposition (HHD) (81) on this vector field to reconstruct the potential energy landscape. Only the energy landscape for x from -100 mm to 100 mm was reconstructed because our landscape model did not capture the beam bouncing back after that range. To roughly unify the input data along the three axes, we multiplied a ratio of 0.01 to the input bases \mathbf{x} along x axis and multiplied the reciprocals of this ratio to the input vectors $f(\mathbf{x})$ along x axis so that the multiplication of the unit of base and vectors – the potential energy – was unchanged. We chose a commonly used Gaussian kernel function $\phi_i(\mathbf{x}) = \exp(-\sigma r_i(\mathbf{x})^2)$, where $r_i(\mathbf{x})$ was the Euclidean distance between the base \mathbf{x} and the i -th center in the unified x - α - β space, because this kernel function fit the expected continuous, 1-order smooth, non-periodic landscape. We generated the $k = 2000$ centers by performing k-means clustering on the input base \mathbf{x} . This kernel number k allows robust estimation results (from a preliminary test, no significant performance reduction with even 60% data loss). We rejected any

centers close to any input base x ($< 10^{-4}$ unit) to avoid singularity in calculation. See Section **S5** for algorithm details.

Comparison criteria and statistics

When comparing the measured data or reconstructed landscape with the model, we were only interested in the period when the robot interacted with the beam obstacles. Here, we defined two fore-aft positions: the attach position x_a , where the robot first contacted all the beams, and the detach position x_d , where the robot first detached from one of the beams and the beam bounced back. For each trial, the attach position x_a was identified as x at the first time frame where both the beam angles θ are bigger than a threshold of 3° ; the detach position x_d was identified as x at the first time frame where either of the beam angle θ reached maximum.

To compare fore-aft force F_x , roll torque T_α , and pitch torque T_β to the model, we only chose the data from the attach position x_a to the detach position x_d . We averaged the absolute difference between the measured data and model over x and divided it by the maximum range of the model data to obtain a relative error:

$$\varepsilon = \frac{|y(x) - r(x)|}{r(x)_{\max} - r(x)_{\min}} \times 100\%,$$

where ε was the relative error, $y(x)$ was the measured data, and $r(x)$ was the model as reference. We used this criterion instead of a traditional relative error definition because the model data had near-zero sections. To compare the measured potential energy landscape in x - α - β space to the model, we flattened the landscapes into 1-D (i.e., function “reshape” in MATLAB) and defined the relative error the same as above. To compare the measured landscape gradients in x - α - β space to the model, we first unify the data along the three axes by dividing the gradients along the x direction by 0.01 (see Section **Potential energy landscape reconstruction** in **Materials and Methods**), then flattened the gradients into a row of vectors (i.e., function “reshape” in MATLAB), and defined the relative error using the maximum norm of model data as the denominator:

$$\varepsilon = \frac{|\overline{y(x)} - r(x)|}{|r(x)|_{max}} \times 100\%.$$

All average data are reported as mean \pm 1 standard deviation. We used a Student’s t-test or a Kruskal-Wallis test to test whether the normal forces and torques or increasing head oscillation frequencies enabled a better estimation of the landscape gradients and landscape reconstruction performance. All the analyses except for statistical tests were performed using MATLAB R2021b (MathWorks, MA). All the statistical tests were performed using JMP PRO 17 (SAS Institute Inc., NC).

Acknowledgments

We thank Ratan Othayoth for sharing CAD files for previous robot system design and discussion on experiment conduction; Xiao Yu for help in assembling the experimental setup and preliminary testing; Qihan Xuan for discussion on experiment design and conduction; Shai Revzen for discussion on experiment design and saddle finding algorithms; Ioannis Kevrekidis, and Anastasia Georgiou for discussions on saddle finding algorithms; Noah Cowan, Jean-Michel Mongeau, Jeremy Brown, and Mitra Hartmann for discussion on active sensing; Mark Nelson and Malcolm MacIver for discussion on sensory acquisition in active sensing systems.

Funding

This work was supported by a Beckman Young Investigator Award from Arnold and Mabel Beckman Foundation for CL, a Career Award at the Scientific Interface from Burroughs Wellcome Fund for CL, a Bridge Grant from Johns Hopkins University Whiting School of Engineering for CL, and a Research Experience for Undergraduates in Computational Sensing and Medical Robotics (CSMR REU) from National Science Foundation for LX and CL.

Author contributions

Y.W. and C.L. designed research; Y.W. performed research; L.X. contributed new methods; Y.W. analyzed data; and Y.W. and C.L. wrote the paper.

Competing interests

Authors declare that they have no competing interests.

Data and materials availability

Robot and experimental system's CAD models, control codes, and experiment data are available from GitHub: https://github.com/TerradynamicsLab/landscape_reconstruct.

Supplementary Material

S1. Potential energy landscape modeling

To theoretically generate the potential energy landscape as ground truth, we approximated the robot's shell as its uncropped counterpart. The robot's center of mass $m = 0.53$ kg was assumed to be at $h = 8$ mm below the geometric center, similar to that of the previous study (31). Each beam was modeled as a massless rigid rectangular plate on a preloaded Hookean torsional joint without damping. For a given robot position and orientation, each beam's deflection angle was calculated as the largest possible forward deflection angle that let the beam contact with the robot, or zero if no such angle existed. Therefore, the beam deflection angles and the elastic potential energy fully depended on the robot's position and orientation. As the system potential energy is the sum of the gravitational potential energy of the robot, the elastic potential energy from the beam, the potential energy landscape depended on the robot's position (x, y, z) and orientation (roll α , pitch β , yaw γ). To calculate the landscape gradients, we took a central differentiation of the potential energy landscape along $\{x, y, z, \alpha, \beta, \gamma\}$ with a 10^{-4} unit perturbation.

S2. Proof that obstacle contact force and torque are negative potential energy landscape gradients

In this proof, we assume that the robot and obstacles move quasi-statically, and there was no friction or damping. The system has no kinetic energy, and the input work all transformed into potential energy:

$$W = \Delta PE,$$

where W is the input work, and ΔPE is the change of the system's potential energy. Examples of the input work are the propulsion from legs or air thrusters. As the robot moves quasi-statically, the equilibrium equations hold:

$$F_{G, q_i} + F_{B, q_i} + F_{W, q_i} = 0, q_i \in \{x, y, z, \alpha, \beta, \gamma\},$$

where F_{G, q_i} , F_{B, q_i} , and F_{W, q_i} are the gravitational, obstacle contact, and external input forces or torques along x, y, z, α, β , or γ axes, separately. The external input force and torque are the partial derivatives of the input work:

$$F_{W, q_i} = \frac{\partial W}{\partial q_i}.$$

We get that the negative gradients of the potential energy is the sum of gravitational and obstacle contact forces or torques:

$$\frac{\partial PE}{\partial q_i} = -(F_{G, q_i} + F_{B, q_i}).$$

We assume that the robot's position and orientation are sensible. Gravitational force and torque can be obtained. We can calculate the obstacle contact force and torque as follows:

$$F_{B, q_i} = -\left(\frac{\partial PE}{\partial q_i} + F_{G, q_i}\right), q_i \in \{x, y, z, \alpha, \beta, \gamma\},$$

which supports our argument that the obstacle contact force and torque is the negative potential energy landscape gradients, biased by the gravitational force and torque.

Note that although the contact forces and torques are the negative gradients of the potential energy from the obstacle ($F_{B, q_i} = -\frac{\partial PE_B}{\partial q_i}$) for this beam traversal problem, this does not apply to other obstacle traversal problems, e.g., in the bump (34), gap (33), and pillar (32) traversal, where the obstacle does not possess potential energy.

S3. Potential energy landscape based on geometry

To examine whether force and torque sensing enabled a potential energy landscape reconstruction better than geometry-based sensing, we generated a potential energy landscape assuming the beams were rigidly fixed, which should be the landscape reconstructed from a perfect geometry-based sensing. Here, if we still assumed that the robot only moved in x - α - β space, we cannot appropriately define a finite potential energy when the robot had to penetrate a beam. Instead, we assumed that the robot adjusted its vertical position z to avoid the beams. The robot's gravitational potential energy at the minimum possible z was defined as the system's potential energy.

S4. Robot design and manufacturing

System design. The experiment system (**Fig. 3A**) consisted of the robotic physical model (**Fig. 3B**), a vertical gantry crane structure (outside **Fig. 3A**) that actuated the robot to move along the fore-aft (x -axis) and vertical (z -axis) directions, and two flexible beams (**Fig. 3A**, green), whose bases moved along the lateral (y -axis) direction. The robot had a body and a head (**Fig. 3B**). The body consisted of a frame, a gyroscope mechanism, and links to control rotation. The head consisted of a frame, two pieces of front shell, two custom 3-axis force sensors (**Fig. 3B**, magenta), and a self-designed data acquisition board (DAQ, **Fig. 3B**, green).

The shell was cropped from a shield-shaped counterpart (**Fig. 3C**, semi-translucent green), whose geometric centers were at the robot's origin at zero head angle. The shell was separated from the middle, which ensured that each part of the front shell only contacted one of the beams. Only the beam-contactable area and a small outer margin were reserved. To best compare with the previous study (31), the axle lengths of the shell's counterpart were kept the same with the previous design.

The two beams were made and characterized using the same method as in (31). Each beam was a rigid acrylic plate (30 mm width \times 200 mm height) attached to the base via a 3-D printed torsional spring joint. The beams only allowed forward deflection. The stiffest beams in (31) were used to maximize the beam contact forces and the force sensors' signal-to-noise ratio.

Actuation. The robot was fully actuated to rotate along pitch and roll direction (Euler angle, Z-Y'-X'' Tait-Bryan convention) and oscillate its head. To easily control the robot to rotate to the desired pitch and roll angles, we designed a gyroscope mechanism at the robot's origin of the body frame and added two servo motors (DYNAMIXEL XC330-M288-T, ROBOTIS Co., South Korea) to separately control the roll (**Fig. 3A, B**, red) and pitch angles (**Fig. 3A, B**, blue). To enable head oscillation, we connected the body frame and the head frame via a servo motor (DYNAMIXEL XC330-M288-T, **Fig. 3A, B**, orange) and used its encoder to monitor the head oscillation angle with a precision of 0.1° . The vertical gantry crane structure's two directions of motion and beam bases' motion were each powered by a servo motor (DYNAMIXEL XM430-W210-T, ROBOTIS Co., South Korea) via a gear-rack mechanism, and the motors' encoders directly obtained the displacements with a precision of 0.01 mm. All the servo motors were commended and reported their rotation angles to a microcontroller (OpenCM 9.04, ROBOTIS Co., South Korea) at a frequency of 50 Hz.

Data collection. To obtain contact force with the obstacles, the load cells with a range of ± 20 N and a precision of ± 0.004 N (BF-02088B, HK Bingf Sci. & Technol. Corp., China) in custom 3-D force sensor were read by the load cell amplifier chips (HX711, Avia Semiconductor, China) on the DAQ board. To obtain contact position, the touch sensory cells were connected to capacitive touch sensor chips (MPR121, Freescale Semiconductor, TX) on the DAQ board via a single wire and a pull-up resistor. When a cell contacted the grounded beam surface, the capacitive touch sensor detected the touch as a voltage drop. To monitor robot's rotation, we put an inertial measurement unit (IMU, **Fig. 3B**, cyan, BNO055, Adafruit Industries, NY) on the robot body and connected it with the DAQ board. A preliminary test showed that the IMU provided a good rotation measurement with errors $< 8^\circ$ and $< 2^\circ$ roll and pitch directions, separately. All the contact force and position and robot rotation sensory data were gathered by a microcontroller (Teensy 4.0, PJRC, OR) on the DAQ board at a frequency of 50 Hz.

The robot was attached to the vertical gantry crane structure via an extra custom 3-D force sensor to monitor the hanging and propelling force. The force sensor consists of three load cells (5kg load cell,

ShangHJ, China) serially connected and orthogonal to each other. With the load cell amplifier chip (HX711), each load cell could provide a separate force measurement along the lab x -, y -, or z -axis, with a range of ± 50 N and a precision of ± 0.02 N. To measure the beam deflection angles, we attached a potentiometer (100 K Ohm Potentiometer, HiLetgo, China) at each beam's rotational joint via a parallel four-bar linkage. The two end terminals were powered at 5 Volt, and the voltage at the wiper was measured to calculate the rotation angle with a precision of 0.3° . The force sensory data from the top sensor and the beam angles were collected by a microcontroller (Arduino Mega, Arduino, Italy) at a frequency of 50 Hz.

Calibration. We calibrated each load cell by rotating it to point $\pm x$ -, $\pm y$ -, $\pm z$ - axes vertically down and hanging various known mass on it. The slope between the applied force and the readout from DAQ was calculated from a linear fit. Because the bias shifted everytime the DAQ restarted, we zeroed all force sensors before each trial of experiments. We characterized torsional stiffness and preload of the beams by measuring the restoring torque about the joint as a function of joint deflection angle using a 3-axis force sensor (Optoforce OMD-20-FG, OnRobot, Denmark), similar to (31). Torsional stiffness and preload of either beam were calculated from the slope and the intercept of the linear fit of the torque as a function of the deflection angle, which was $285 \text{ N}\cdot\text{mm}\cdot\text{rad}^{-1}$ and $91 \text{ N}\cdot\text{mm}$ for the left beam and $324 \text{ N}\cdot\text{mm}\cdot\text{rad}^{-1}$ and $77 \text{ N}\cdot\text{mm}$ for the right beam.

Visualization. We used a LabVIEW program to bidirectionally communicate with the microcontrollers and record experimental data at a frequency of 50 Hz. The LabVIEW graphical user interface (GUI, see supplementary video) allowed us to check all the sensory information (i.e., the robot's position, orientation, head oscillation angle, force amplitudes and contact positions on each piece of front shell, propelling force, and the beams' positions and deflection angles), manually control the system, and conduct automatic pre-programmed experiments.

S5. Meshless Helmholtz-Hodge decomposition

The idea of Helmholtz-Hodge decomposition (82) was to consider the vector field as a sum of a gradient vector field (i.e., curl-free) and a solenoidal vector field (i.e., divergence-free):

$$f(\mathbf{x}) = g(\mathbf{x}) + r(\mathbf{x}) = -\nabla\Phi + \nabla \times A,$$

where \mathbf{x} was the independent variable vector, or the base of vectors (e.g., $\mathbf{x} = [x, \alpha, \beta]$ in our problem), $g(\mathbf{x})$ was the gradient vector of a scalar potential Φ , $r(\mathbf{x})$ was the solenoidal vector, which was a curl of the vector potential A . We used the scalar potential Φ as the estimated potential energy landscape.

In meshless Helmholtz-Hodge decomposition (81), the scalar potential Φ and the vector potential A were approximated as a linear combination of kernel function ϕ of a group of scattered points (centers):

$$\Phi = \sum_{i=1}^k a_i \phi_i,$$

$$A = \sum_{i=1}^k [b_{i,1}\phi_i, b_{i,2}\phi_i, b_{i,3}\phi_i]^T = \sum_{i=1}^k (\phi_i I) b_i,$$

where k was the number of centers, ϕ_i was the kernel function at the i -th center, a_i and $b_i = [b_{i,1}, b_{i,2}, b_{i,3}]^T$ were its coefficients of the linear combination, and I was a 3×3 identity matrix. At a given base \mathbf{x} , the gradients $f_g(\mathbf{x})$ and solenoidal $f_s(\mathbf{x})$ vector field were represented by the gradients of kernel function:

$$f_g(\mathbf{x}) = \sum_{i=1}^k a_i \nabla \phi_i = (\nabla \Phi)^T a,$$

$$\text{where } \nabla \Phi := [\nabla \phi_1, \dots, \nabla \phi_k]^T, a := [a_1, \dots, a_k]^T,$$

$$f_s(\mathbf{x}) = \sum_{i=1}^k \nabla \times \phi_i I b_i = (\nabla \times \Phi I)^T b,$$

$$\text{where } \nabla \times \Phi I := \begin{bmatrix} \nabla \times \phi_1 I \\ \dots \\ \nabla \times \phi_k I \end{bmatrix}_{3k \times 3}, b := [b_{1,1}, b_{1,2}, b_{1,3}, \dots, \dots, b_{k,1}, b_{k,2}, b_{k,3}]^T.$$

We speculate that the meshless landscape reconstruction algorithm we applied suits applications of a legged mobile robot that moves on cluttered terrain. In these cases, the robot's motion is also affected by the interaction with the obstacles, and the robot usually cannot freely and systematically vary its translation or rotation. The force sensory data can be heterogeneously scattered in the state space and sometimes missing in time series, which hinders applying some reconstruction algorithms (83–87) that need evenly distributed data. In contrast, the nature of the meshless algorithm handles the fragmented sensory data and allows for reconstructing the landscape locally in the state space, which is sufficient for most state-feedback controllers.

S6. Choosing head oscillation frequency

We designed the robot’s head oscillation frequency based on the observed animal behavior (35). When exploring around and negotiating between the beams, the cockroach actively oscillated its head in a changing frequency (**Fig. 1G, Fig. 1H**). To obtain an average oscillation frequency, we separated each head oscillation cycle into two phases – the lowering phase, where the head angle increased, and the raising phase, where the head angle decreased. We defined the amplitude as the maximum range of head angles and angular velocity as the fraction of this amplitude over the time span of each phase. The average amplitude and angular velocity were $15^\circ \pm 9^\circ$ and $145^\circ \pm 100^\circ \cdot \text{s}^{-1}$ in the lowering phases and $16^\circ \pm 10^\circ$ and $150^\circ \pm 90^\circ \cdot \text{s}^{-1}$ in the raising phases for all the observed head oscillation cycles (35). Using these data, we calculated the average head oscillation frequency to be roughly 5 Hz for the animals. Because the animal traversed the beam obstacle in 4 ± 1 seconds (35) while the robot used roughly 10 seconds, the robot head oscillation frequency was designed to be 2 Hz to keep the same head oscillation cycle number. We also tried 0.5 Hz and 1 Hz for comparison but did not try higher frequencies due to the speed limit of the servo motor.

S7. Various force sensing data observed in repeated experiments

Although our data showed consistency for repeated experiments (x -average coefficient of variation = $2\% \pm 1\%$ for F_x , $2\% \pm 2\%$ for T_α , $3\% \pm 3\%$ for T_β . See how we averaged the repeated trials in Section *Data filtering and averaging* in *Materials and Methods*), we also found that the result was various of some roll and pitch combinations when the head oscillation was involved (maximum coefficient of variation = $20\% \pm 9\%$ for F_x , $24\% \pm 6\%$ for T_α , $27\% \pm 5\%$ for T_β), probably due to the random starting phase of the head oscillation (see Section *Robot experiment protocol* and Section *Data filtering and averaging* in *Materials and Methods*). These trials[†] were mostly (86%) of the roll and pitch combination near the separatrix. We carefully watched the video recording of these trials and speculated that some were caused by head-oscillation-induced pitch-to-roll transition or sudden beam bouncing back.

[†] For $f = 0.5$ Hz, $\{\alpha, \beta\} = \{35^\circ, 10^\circ\}$; for $f = 1$ Hz, $\{\alpha, \beta\} = \{35^\circ, 10^\circ\}, \{40^\circ, 15^\circ\}, \{40^\circ, 25^\circ\}, \{30^\circ, 20^\circ\}$; for $f = 2$ Hz, $\{\alpha, \beta\} = \{35^\circ, 10^\circ\}, \{30^\circ, 20^\circ\}$.

Supplementary figures and tables

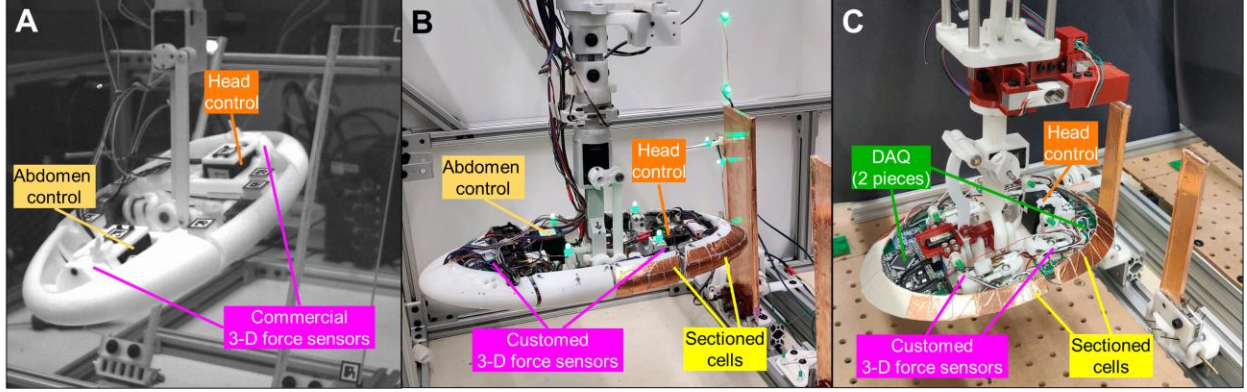


Fig. S1. Iterative development of robots to enable force and contact measurement. (A) The first iteration. The robot was capable of head and abdomen oscillation and contact force sensing using commercial 3-D force sensors. This robot cannot sense the contact position nor separate the contact force with either beam, because the commercial 3-D force sensors were too bulky to place multiple of them in the confined space near head. (B) The second iteration. The commercial 3-D force sensors were replaced with small, low-cost, custom-made ones. The head, body, and abdomen were separated from the middle so that the force sensors could individually sense the contact force from either beam. Sectioned cells were planted on the robot's head and front body surfaces to enable contact position sensing. The robot often suffered from signal loss issues due to the long wiring to a DAQ board far from it. (C) The third iteration. To make the robot the same size and shape as in the previous study (31), the body and abdomen were merged, and the shell was designed to be shield-shaped. Customized DAQ boards were deployed to reduce wiring and signal transmission issues. The robot was damaged once the gap between the head and body was caught by a beam.

Table 1. Relative error in estimating forces, torques, landscape potential energy, and gradients.

Variable		F_x	T_α	T_β	Potential Energy	Gradients
$f = 0$ Hz	Raw	$16\% \pm 3\%$	$19\% \pm 28\%$	$25\% \pm 9\%$	$14.03\% \pm 0.03\%$	$21.6\% \pm 0.7\%$

	Normal	5% \pm 3%	19% \pm 28%	31% \pm 9%	7.24% \pm 0.02%	17.7% \pm 0.4%
	Model	-	-	-	2.09% \pm 0.05%	12.5% \pm 0.9%
$f = 0.5$ Hz	Raw	20% \pm 5%	18% \pm 21%	31% \pm 13%	17.77% \pm 0.03%	24.4% \pm 0.9%
$f = 1$ Hz	Raw	19% \pm 6%	18% \pm 17%	28% \pm 13%	17.01% \pm 0.01%	23.5% \pm 0.2%
$f = 2$ Hz	Raw	13% \pm 4%	17% \pm 15%	22% \pm 7%	11.14% \pm 0.04%	18.9% \pm 0.3%

All data averages are mean \pm 1 standard deviation.

Video 1. Robot experiment recording and evolution of reconstructed potential energy landscape. (1 and **2)** Video recording of robot experiments (left) and real-time data visualization (right). (1) Head was static. (2) Head was oscillated at 2 Hz. (3) Evolution of reconstructed potential energy landscape (top) as the robot moved forward, compared with ground truth (bottom).

References

1. B. Ranft, C. Stiller, The Role of Machine Vision for Intelligent Vehicles. *IEEE Trans. Intell. Veh.* **1**, 8–19 (2016).
2. H. Durrant-Whyte, T. Bailey, Simultaneous localization and mapping: part I. *IEEE Robot. Autom. Mag.* **13**, 99–110 (2006).
3. J. A. Castellanos, J. M. M. Montiel, J. Neira, J. D. Tardos, The SPmap: a probabilistic framework for simultaneous localization and map building. *IEEE Trans. Robot. Autom.* **15**, 948–952 (1999).
4. M. W. M. G. Dissanayake, P. Newman, S. Clark, H. F. Durrant-Whyte, M. Csorba, A solution to the simultaneous localization and map building (SLAM) problem. *IEEE Trans. Robot. Autom.* **17**, 229–241 (2001).
5. M. Montemerlo, S. Thrun, D. Koller, B. Wegbreit, “FastSLAM: A Factored Solution to the Simultaneous Localization and Mapping Problem” in *Proceedings of the 18th National Conference on Artificial Intelligence (AAAI)* (2002), pp. 593–598.

6. S. Thrun, W. Burgard, D. Fox, “A real-time algorithm for mobile robot mapping with applications to multi-robot and 3D mapping” in *Proceedings 2000 ICRA. Millennium Conference. IEEE International Conference on Robotics and Automation. Symposia Proceedings (Cat. No.00CH37065)* (IEEE, 2000)vol. 1, pp. 321–328.
7. D. E. Koditschek, E. Rimon, Robot navigation functions on manifolds with boundary. *Adv. Appl. Math.* **11**, 412–442 (1990).
8. E. Rimon, D. E. Koditschek, Exact robot navigation using artificial potential functions. *IEEE Trans. Robot. Autom.* **8**, 501–518 (1992).
9. O. Khatib, “Real-time obstacle avoidance for manipulators and mobile robots” in *Proceedings. 1985 IEEE International Conference on Robotics and Automation* (Institute of Electrical and Electronics Engineers, 1985)vol. 2, pp. 500–505.
10. S. Thrun, Toward robotic cars. *Commun. ACM* **53**, 99–106 (2010).
11. A. Sgorbissa, R. Zaccaria, Planning and obstacle avoidance in mobile robotics. *Rob. Auton. Syst.* **60**, 628–638 (2012).
12. G. Bellegarda, A. Ijspeert, Visual CPG-RL: Learning Central Pattern Generators for Visually-Guided Quadruped Navigation. *arXiv*, 2212.14400v1 [cs.RO] (2022).
13. O. Arslan, V. Pacelli, D. E. Koditschek, “Sensory steering for sampling-based motion planning” in *2017 IEEE/RSJ International Conference on Intelligent Robots and Systems (IROS)* (IEEE, 2017)vols. 2017-Septe, pp. 3708–3715.
14. P. Holmes, R. J. Full, D. Koditschek, J. Guckenheimer, The Dynamics of Legged Locomotion: Models, Analyses, and Challenges. *SIAM Rev.* **48**, 207–304 (2006).
15. A. A. Biewener, M. A. Daley, Unsteady locomotion: integrating muscle function with whole body dynamics and neuromuscular control. *J. Exp. Biol.* **210**, 2949–2960 (2007).

16. S. Revzen, S. A. Burden, T. Y. Moore, J.-M. Mongeau, R. J. Full, Instantaneous kinematic phase reflects neuromechanical response to lateral perturbations of running cockroaches. *Biol. Cybern.* **107**, 179–200 (2013).
17. A. V. Birn-Jeffery, C. M. Hubicki, Y. Blum, D. Renjewski, J. W. Hurst, M. A. Daley, Don't break a leg: running birds from quail to ostrich prioritise leg safety and economy on uneven terrain. *J. Exp. Biol.* **217**, 3786–3796 (2014).
18. D. E. Koditschek, R. J. Full, M. Buehler, Mechanical aspects of legged locomotion control. *Arthropod Struct. Dev.* **33**, 251–272 (2004).
19. S. Sponberg, R. J. Full, Neuromechanical response of musculo-skeletal structures in cockroaches during rapid running on rough terrain. *J. Exp. Biol.* **211**, 433–446 (2008).
20. A. J. Spence, S. Revzen, J. Seipel, C. Mullens, R. J. Full, Insects running on elastic surfaces. *J. Exp. Biol.* **213**, 1907–1920 (2010).
21. G. Clifton, A. Y. Stark, C. Li, N. Gravish, The bumpy road ahead: the role of substrate roughness on animal walking and a proposed comparative metric. *J. Exp. Biol.* **226** (2023).
22. J. Whitman, N. Zevallos, M. Travers, H. Choset, “Snake Robot Urban Search After the 2017 Mexico City Earthquake” in *2018 IEEE International Symposium on Safety, Security, and Rescue Robotics (SSRR)* (IEEE, 2018), pp. 1–6.
23. R. R. Murphy, “Disaster robotics” in *Springer Handbook of Robotics*, B. Siciliano, O. Khatib, Eds. (MIT press, 2014).
24. T. Miki, J. Lee, J. Hwangbo, L. Wellhausen, V. Koltun, M. Hutter, Learning robust perceptive locomotion for quadrupedal robots in the wild. *Sci. Robot.* **7** (2022).
25. J. Lee, J. Hwangbo, L. Wellhausen, V. Koltun, M. Hutter, Learning quadrupedal locomotion over challenging terrain. *Sci. Robot.* **5** (2020).

26. R. E. Arvidson, J. F. Bell, P. Bellutta, N. A. Cabrol, J. G. Catalano, J. Cohen, L. S. Crumpler, D. J. Des Marais, T. A. Estlin, W. H. Farrand, R. Gellert, J. A. Grant, R. N. Greenberger, E. A. Guinness, K. E. Herkenhoff, J. A. Herman, K. D. Iagnemma, J. R. Johnson, G. Klingelhöfer, R. Li, K. A. Lichtenberg, S. A. Maxwell, D. W. Ming, R. V. Morris, M. S. Rice, S. W. Ruff, A. Shaw, K. L. Siebach, P. A. de Souza, A. W. Stroupe, S. W. Squyres, R. J. Sullivan, K. P. Talley, J. A. Townsend, A. Wang, J. R. Wright, A. S. Yen, Spirit Mars Rover Mission: Overview and selected results from the northern Home Plate Winter Haven to the side of Scamander crater. *J. Geophys. Res. Planets* **115**, 1–19 (2010).
27. P. C. Leger, A. Trebi-Ollennu, J. R. Wright, S. A. Maxwell, R. G. Bonitz, J. J. Biesiadecki, F. R. Hartman, B. K. Cooper, E. T. Baumgartner, M. W. Maimone, “Mars Exploration Rover Surface Operations: Driving Spirit at Gusev Crater” in *2005 IEEE International Conference on Systems, Man and Cybernetics* (IEEE, 2005)vol. 2, pp. 1815–1822.
28. C. Li, K. Lewis, The Need for and Feasibility of Alternative Ground Robots to Traverse Sandy and Rocky Extraterrestrial Terrain. *Adv. Intell. Syst.* **5**, 1–8 (2023).
29. C. Li, A. O. Pullin, D. W. Haldane, H. K. Lam, R. S. Fearing, R. J. Full, Terradynamically streamlined shapes in animals and robots enhance traversability through densely cluttered terrain. *Bioinspir. Biomim.* **10**, 046003 (2015).
30. R. Othayoth, Q. Xuan, Y. Wang, C. Li, Locomotor transitions in the potential energy landscape-dominated regime. *Proc. R. Soc. B Biol. Sci.* **288**, rspb.2020.2734 (2021).
31. R. Othayoth, G. Thoms, C. Li, An energy landscape approach to locomotor transitions in complex 3D terrain. *Proc. Natl. Acad. Sci.* **117**, 14987–14995 (2020).
32. Y. Han, R. Othayoth, Y. Wang, C.-C. Hsu, R. de la Tijera Obert, E. Francois, C. Li, Shape-induced obstacle attraction and repulsion during dynamic locomotion. *Int. J. Rob. Res.* **40**, 939–955 (2021).

33. S. W. Gart, C. Yan, R. Othayoth, Z. Ren, C. Li, Dynamic traversal of large gaps by insects and legged robots reveals a template. *Bioinspir. Biomim.* **13**, 026006 (2018).
34. S. W. Gart, C. Li, Body-terrain interaction affects large bump traversal of insects and legged robots. *Bioinspir. Biomim.* **13**, 026005 (2018).
35. Y. Wang, R. Othayoth, C. Li, Cockroaches adjust body and appendages to traverse cluttered large obstacles. *J. Exp. Biol.* **225** (2022).
36. A. H. A. Al-dabbagh, R. Ronsse, A review of terrain detection systems for applications in locomotion assistance. *Rob. Auton. Syst.* **133**, 103628 (2020).
37. H. B. Schlegel, Following gradient extremal paths. *Theor. Chim. Acta* **83**, 15–20 (1992).
38. C. M. Smith, How to find a saddle point. *Int. J. Quantum Chem.* **37**, 773–783 (1990).
39. J. Tsitsiklis, D. Bertsekas, M. Athans, Distributed asynchronous deterministic and stochastic gradient optimization algorithms. *IEEE Trans. Automat. Contr.* **31**, 803–812 (1986).
40. D. Biswas, A. Lamperski, Y. Yang, K. Hoffman, J. Guckenheimer, E. S. Fortune, N. J. Cowan, Mode switching in organisms for solving explore-versus-exploit problems. *Nat. Mach. Intell.*, doi: 10.1038/s42256-023-00745-y (2023).
41. J. Aguilar, T. Zhang, F. Qian, M. Kingsbury, B. McInroe, N. Mazouchova, C. Li, R. Maladen, C. Gong, M. Travers, R. L. Hatton, H. Choset, P. B. Umbanhowar, D. I. Goldman, A review on locomotion robophysics: the study of movement at the intersection of robotics, soft matter and dynamical systems. *Reports Prog. Phys.* **79**, 110001 (2016).
42. A. J. Ijspeert, Biorobotics: Using robots to emulate and investigate agile locomotion. *Science* **346**, 196–203 (2014).
43. Y. O. Aydin, J. M. Rieser, C. M. Hubicki, W. Savoie, D. I. Goldman, “Physics approaches to

- natural locomotion: Every robot is an experiment” in *Robotic Systems and Autonomous Platforms* (Elsevier, 2019), pp. 109–127.
44. Q. Fu, C. Li, Robotic modelling of snake traversing large, smooth obstacles reveals stability benefits of body compliance. *R. Soc. Open Sci.* **7**, 191192 (2020).
 45. Q. Fu, “Snake and snake robot locomotion in complex, 3-d terrain,” Johns Hopkins University (2023).
 46. G. V. Lauder, Robotics as a Comparative Method in Ecology and Evolutionary Biology. *Integr. Comp. Biol.* **62**, 721–734 (2022).
 47. N. Gravish, G. V. Lauder, Robotics-inspired biology. *J. Exp. Biol.* **221**, 1–8 (2018).
 48. B. Webb, What does robotics offer animal behaviour? *Anim. Behav.* **60**, 545–558 (2000).
 49. A. J. Ijspeert, M. A. Daley, Integration of feedforward and feedback control in the neuromechanics of vertebrate locomotion: a review of experimental, simulation and robotic studies. *J. Exp. Biol.* **226** (2023).
 50. Y. Xian, C. H. Lampert, B. Schiele, Z. Akata, Zero-Shot Learning—A Comprehensive Evaluation of the Good, the Bad and the Ugly. *IEEE Trans. Pattern Anal. Mach. Intell.* **41**, 2251–2265 (2019).
 51. F. Qian, D. Goldman, “Anticipatory control using substrate manipulation enables trajectory control of legged locomotion on heterogeneous granular media” in *Micro- and Nanotechnology Sensors, Systems, and Applications VII*, T. George, A. K. Dutta, M. S. Islam, Eds. (2015) vol. 9467, p. 94671U.
 52. T. J. Prescott, M. E. Diamond, A. M. Wing, Active touch sensing. *Philos. Trans. R. Soc. B Biol. Sci.* **366**, 2989–2995 (2011).

53. D. Biswas, L. A. Arend, S. A. Stamper, B. P. Vágvölgyi, E. S. Fortune, N. J. Cowan, Closed-Loop Control of Active Sensing Movements Regulates Sensory Slip. *Curr. Biol.* **28**, 4029-4036.e4 (2018).
54. Y. Baba, A. Tsukada, C. M. Comer, Collision avoidance by running insects: antennal guidance in cockroaches. *J. Exp. Biol.* **213**, 2294–2302 (2010).
55. J. Okada, Y. Toh, Active tactile sensing for localization of objects by the cockroach antenna. *J. Comp. Physiol. A* **192**, 715–726 (2006).
56. C. Schütz, V. Dürr, Active tactile exploration for adaptive locomotion in the stick insect. *Philos. Trans. R. Soc. B Biol. Sci.* **366**, 2996–3005 (2011).
57. V. Berendes, V. Dürr, Active tactile exploration and tactually induced turning in tethered walking stick insects. *J. Exp. Biol.* **225** (2022).
58. R. Othayoth, B. Strebel, Y. Han, E. Francois, C. Li, A terrain treadmill to study animal locomotion through large obstacles. *J. Exp. Biol.* **225** (2022).
59. M. J. Hartmann, Active sensing capabilities of the rat whisker system. *Auton. Robots* **11**, 249–254 (2001).
60. N. O. Zweifel, M. J. Z. Hartmann, Defining “active sensing” through an analysis of sensing energetics: homeoactive and alloactive sensing. *J. Neurophysiol.* **124**, 40–48 (2020).
61. N. E. Bush, S. A. Solla, M. J. Hartmann, Whisking mechanics and active sensing. *Curr. Opin. Neurobiol.* **40**, 178–188 (2016).
62. M. J. Z. Hartmann, A night in the life of a rat: Vibrissal mechanics and tactile exploration. *Ann. N. Y. Acad. Sci.* **1225**, 110–118 (2011).
63. A. E. Schultz, J. H. Solomon, M. A. Peshkin, M. J. Hartmann, Multifunctional whisker arrays for

- distance detection, terrain mapping, and object feature extraction. *Proc. - IEEE Int. Conf. Robot. Autom.* **2005**, 2588–2593 (2005).
64. J. H. Solomon, M. J. Z. Hartmann, Extracting object contours with the sweep of a robotic whisker using torque information. *Int. J. Rob. Res.* **29**, 1233–1245 (2010).
 65. H. M. Emmett, M. M. Graff, M. J. Z. Hartmann, A Novel Whisker Sensor Used for 3D Contact Point Determination and Contour Extraction. *Robot. Sci. Syst.*, doi: 10.15607/RSS.2018.XIV.059 (2018).
 66. L. A. Huet, J. W. Rudnicki, M. J. Z. Hartmann, Tactile sensing with whiskers of various shapes: Determining the three-dimensional location of object contact based on mechanical signals at the whisker base. *Soft Robot.* **4**, 88–102 (2017).
 67. L. A. Huet, H. M. Emmett, M. J. Z. Hartmann, Demonstration of three-dimensional contact point determination and contour reconstruction during active whisking behavior of an awake rat. *PLoS Comput. Biol.* **18**, 1–28 (2022).
 68. J. Mi, Y. Wang, C. Li, “Omni-Roach: A Legged Robot Capable of Traversing Multiple Types of Large Obstacles and Self-Righting” in *2022 International Conference on Robotics and Automation (ICRA)* (IEEE, 2022), pp. 235–242.
 69. W. J. Bell, L. M. Roth, C. A. Nalepa., *Cockroaches: Ecology, Behavior, and Natural History* (John Hopkins University Press, Baltimore, MD, 2007).
 70. H.-U. Thiele, *Carabid Beetles in Their Environments: A Study on Habitat Selection by Adaptations in Physiology and Behaviour* (Springer Science & Business Media, Berlin, Heidelberg, New York, 1977).
 71. J. C. Tuthill, E. Azim, Proprioception. *Curr. Biol.* **28**, R194–R203 (2018).
 72. J. C. Tuthill, R. I. Wilson, Mechanosensation and Adaptive Motor Control in Insects. *Curr. Biol.*

- 26**, R1022–R1038 (2016).
73. G. Henkelman, G. Jóhannesson, H. Jónsson, “Methods for Finding Saddle Points and Minimum Energy Paths” in *Theoretical Methods in Condensed Phase Chemistry* (Kluwer Academic Publishers, Dordrecht, 2008), pp. 269–302.
 74. J. M. Bello-Rivas, A. Georgiou, H. Vandecasteele, I. G. Kevrekidis, Gentlest Ascent Dynamics on Manifolds Defined by Adaptively Sampled Point-Clouds. *J. Phys. Chem. B* **127**, 5178–5189 (2023).
 75. L. Zhang, W. Ren, A. Samanta, Q. Du, Recent developments in computational modelling of nucleation in phase transformations. *npj Comput. Mater.* **2**, 16003 (2016).
 76. W. Quapp, M. Hirsch, O. Imig, D. Heidrich, Searching for saddle points of potential energy surfaces by following a reduced gradient. *J. Comput. Chem.* **19**, 1087 (1998).
 77. J. M. Bello-Rivas, A. Georgiou, J. Guckenheimer, I. G. Kevrekidis, Staying the course: iteratively locating equilibria of dynamical systems on Riemannian manifolds defined by point-clouds. *J. Math. Chem.* **61**, 600–629 (2023).
 78. R. W. Pastor, “Techniques and Applications of Langevin Dynamics Simulations” in *The Molecular Dynamics of Liquid Crystals* (Springer Netherlands, Dordrecht, 1994), pp. 85–138.
 79. M. I. Jordan, “Dynamical, symplectic and stochastic perspectives on gradient-based optimization” in *Proceedings of the International Congress of Mathematicians (ICM 2018)* (WORLD SCIENTIFIC, 2019)vol. 1, pp. 523–549.
 80. X. Cheng, D. Yin, P. L. Bartlett, M. I. Jordan, Stochastic Gradient and Langevin Processes. *37th Int. Conf. Mach. Learn. ICML 2020 Part F***16814**, 1788–1797 (2019).
 81. G. Patane, Meshless Approximation and Helmholtz-Hodge Decomposition of Vector Fields. *IEEE Trans. Vis. Comput. Graph.* **28**, 1–14 (2022).

- 82. H. Bhatia, G. Norgard, V. Pascucci, P. T. Bremer, The Helmholtz-Hodge decomposition - A survey. *IEEE Trans. Vis. Comput. Graph.* **19**, 1386–1404 (2013).
- 83. F. H. Razafindrazaka, K. Poelke, K. Polthier, L. Goubergrits, A Consistent Discrete 3D Hodge-type Decomposition: implementation and practical evaluation. (2019).
- 84. A. Lemoine, J. P. Caltagirone, M. Azañez, S. Vincent, Discrete Helmholtz–Hodge Decomposition on Polyhedral Meshes Using Compatible Discrete Operators. *J. Sci. Comput.* **65**, 34–53 (2015).
- 85. E. Deriaz, V. Perrier, Divergence-free and curl-free wavelets in two dimensions and three dimensions: Application to turbulent flows. *J. Turbul.* **7**, 1–37 (2006).
- 86. Q. Guo, M. K. Mandal, M. Y. Li, Efficient Hodge-Helmholtz decomposition of motion fields. *Pattern Recognit. Lett.* **26**, 493–501 (2005).
- 87. D. Q. Nguyen, R. Fedkiw, H. W. Jensen, Physically based modeling and animation of fire. *Proc. 29th Annu. Conf. Comput. Graph. Interact. Tech. SIGGRAPH '02*, 721–728 (2002).